Author/s:
Sefidmooye Azar, N;Bullock, J;Shrestha, VR;Balendhran, S;Yan, W;Kim, H;Javey, A;Crozier, KB

Title:
Long-Wave Infrared Photodetectors Based on 2D Platinum Diselenide atop Optical Cavity Substrates

Date:
2021-04-27

Citation:
Sefidmooye Azar, N., Bullock, J., Shrestha, V. R., Balendhran, S., Yan, W., Kim, H., Javey, A. & Crozier, K. B. (2021). Long-Wave Infrared Photodetectors Based on 2D Platinum Diselenide atop Optical Cavity Substrates. ACS Nano, 15 (4), pp.6573-6581. https://doi.org/10.1021/acsnano.0c09739.

Long-Wave Infrared Photodetectors Based on 2D Platinum Diselenide atop Optical Cavity Substrates

Nima Sefidmooye Azar,[†] James Bullock,[†] Vivek Raj Shrestha,[‡] Sivacarendran Balendhran,[‡] Wei Yan,[†] Hyungjin Kim,[¶,§] Ali Javey,[¶,§] and Kenneth B. Crozier[*,†,‡,‖]

[†]*Department of Electrical and Electronic Engineering, University of Melbourne, Victoria 3010, Australia*

[‡]*School of Physics, University of Melbourne, Victoria 3010, Australia*

[¶]*Department of Electrical Engineering and Computer Sciences, University of California, Berkeley, CA 94720, USA*

[§]*Materials Sciences Division, Lawrence Berkeley National Laboratory, Berkeley, CA 94720, USA*

[‖]*ARC Centre of Excellence for Transformative Meta-Optical Systems, University of Melbourne, Victoria 3010, Australia*

E-mail: kcrozier@unimelb.edu.au

Abstract

Long-wave infrared (LWIR) photodetection is of high technological importance, having a wide range of applications that include thermal imaging and spectroscopy. Two-dimensional (2D) noble-transition-metal dichalcogenides, platinum diselenide ($PtSe_2$)

in particular, have recently shown great promise for infrared detection. However, previous studies have mainly focused on wavelengths up to the short-wave infrared region. In this work, we demonstrate LWIR photodetectors based on multilayer $PtSe_2$. In addition, we present an optical cavity substrate which enhances the light-matter interaction in 2D materials and thus their photodetection performance in the LWIR spectral region. The $PtSe_2$ photoconductors fabricated on the TiO_2/Au optical cavity substrate exhibit responsivities up to 54 mA/W to LWIR illumination at a wavelength of 8.35 μm. Moreover, these devices show a fast photoresponse with a time constant of 54 ns to white light illumination. The findings of this study reveal the potential of multilayer $PtSe_2$ for fast and broadband photodetection from visible to LWIR wavelengths.

Keywords

$PtSe_2$, two-dimensional materials, noble-transition-metal dichalcogenides, light-matter interaction enhancement, light intensity and absorption, IR detectors, fast and broadband photodetection

Infrared (IR) photodetectors play a key role in a variety of areas including biomedical and thermal imaging, telecommunication, gas sensing, surveillance, search and rescue, environmental monitoring, and astronomy.[1] Mercury cadmium telluride (MCT), a composition-tunable direct bandgap semiconductor, has been extensively employed in mid-wave infrared (MWIR, 3–8 μm) and long-wave infrared (LWIR, 8–15 μm) photodetectors.[2,3] Nevertheless, some issues such as difficulty of precise composition control and large-area non-uniformity result in a low-yield and complex fabrication process.[2,4] This has stimulated the search for alternative technologies for IR detection. Two-dimensional (2D) layered materials have been found promising for this purpose.[5–11]

IR photodetectors based on graphene,[12–17] black phosphorus (bP),[18–21] bPAs,[22,23] quasi-2D Te,[24,25] and SeTe[26] have been demonstrated. Recently, 2D noble-transition-metal dichalco-

genides[27] including $PtSe_2$,[28–31] $PdSe_2$,[32–34] and PtS_2[35] have also been explored for IR detection. These materials possess appealing properties such as air stability, which is particularly an issue with bP;[36] thickness-tunable bandgap; and relatively high carrier mobility.[37] Photodiodes based on $PtSe_2$ heterojunctions with Si,[38–40] Ge,[41] CdTe,[42] a perovskite,[43] PtS_2,[44] and GaAs[45] have also been investigated for broadband photodetection up to short-wave infrared (SWIR, 1.4–3 μm) wavelengths.

Ab initio calculations reveal that $PtSe_2$ has a thickness-dependent band structure. Monolayer and bilayer $PtSe_2$ are semiconductors with indirect bandgaps of $\sim$1.2 eV and $\sim$0.3 eV, respectively, and thicker flakes are semi-metallic with zero bandgap.[28,46] Yu *et al.*[28] recently showed that the bandgap of bilayer $PtSe_2$ can be further narrowed to the LWIR region ($\sim$0.11 eV) by introducing Se vacancies in the $PtSe_2$ crystals using a customized chemical vapor transport (CVT) system. Utilizing this material, they achieved a responsivity, detectivity, and rise/fall time of 4.5 A/W, 7×10^8 Jones, and 1.2 ms, respectively, for illumination at a wavelength of 10 μm. Despite the impressive device performance, from a manufacturing standpoint, it may prove challenging to produce $PtSe_2$ bilayers containing Se vacancies of the appropriate density in the reproducible manner required for devices such as image sensors.

In this study, we demonstrate, for the first time to the best of our knowledge, LWIR photodetectors based on multilayer $PtSe_2$. We employ a TiO_2/Au optical cavity substrate to boost the light-matter interaction in $PtSe_2$ and enhance its LWIR detection performance. Optical cavity substrates have been previously used in graphene[47] devices in the MWIR, Te[24] and SeTe[26] devices in the SWIR, and MoS_2[48] devices in the visible spectral regions. Our simulation and experimental results show that the performance of the 2D material-based LWIR detectors can be significantly improved using the optical cavity substrate in comparison with the commonly used SiO_2/Si substrate. Device characterization reveals that the multilayer $PtSe_2$ photodetectors exhibit a fast and broadband photoresponse.

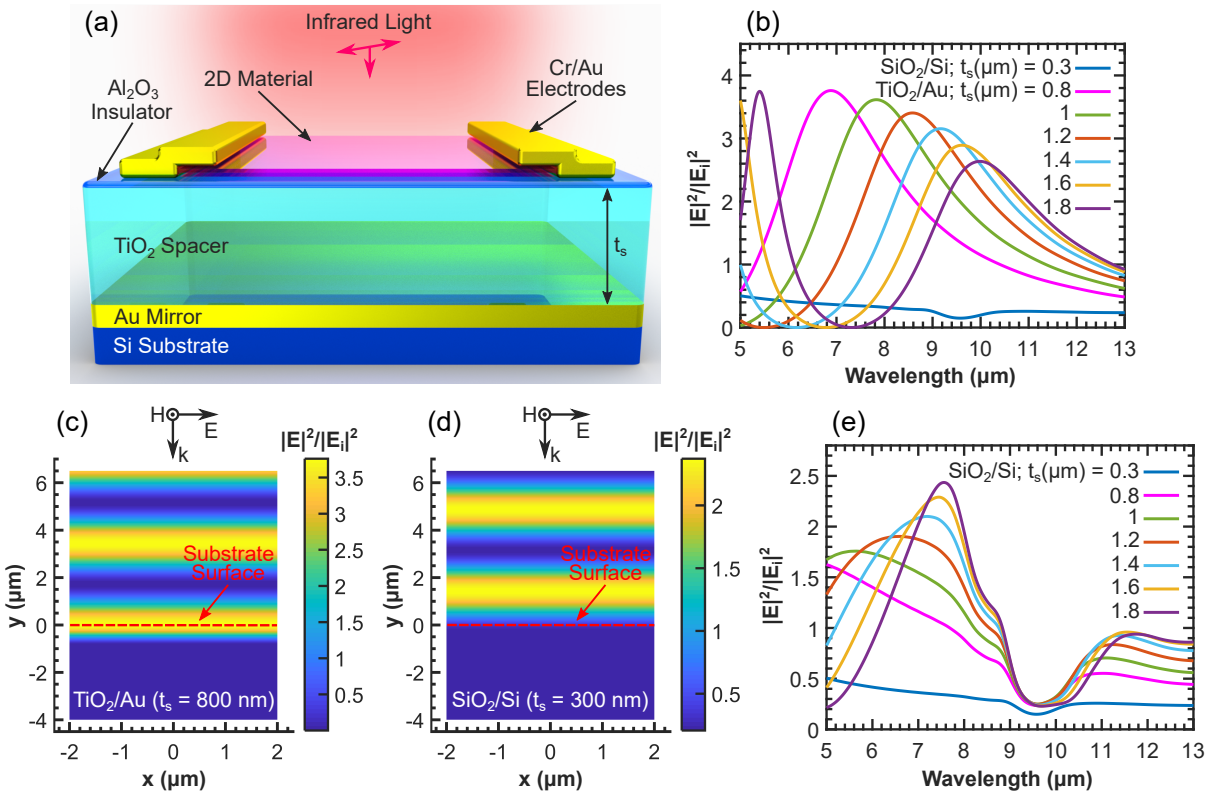

Figure 1: (a) Schematic of the infrared photodetector based on 2D materials atop TiO_2/Au optical cavity substrate. (b) Normalized electric field intensity at the substrate surface in the absence of the 2D material for the SiO_2/Si (t_s = 300 nm) substrate and TiO_2/Au substrate with different spacer thicknesses. (c) and (d) Normalized electric field intensity distribution in the cross section of the TiO_2/Au (t_s = 800 nm) and SiO_2/Si (t_s = 300 nm) substrates, respectively, in the absence of the 2D material at $\lambda = 6.9$ μm. The red dashed line represents the substrate surface which lies at $y = 0$. (e) Same as b for the SiO_2/Si substrate with different SiO_2 thicknesses. E_i is the norm of the incident electric field.

Results and discussion

The structure of the infrared photodetector based on 2D materials atop TiO_2/Au optical cavity substrate is depicted in Figure 1a. The optical cavity substrate consists of a 120-nm-thick Au mirror, a TiO_2 spacer layer with thickness t_s, and a 30-nm-thick Al_2O_3 insulator film on an Si substrate. The reflected light from the Au mirror interferes constructively with the incident light at the substrate surface leading to light intensity enhancement. To maximize the light intensity at the substrate surface at wavelength λ, the spacer thickness (t_s) should be approximately equal to $\lambda/(4n_s)$, where n_s is the refractive index of the spacer. The Al_2O_3

layer electrically insulates the 2D material sitting on the substrate from the spacer/mirror stack. This structure can be simultaneously used to apply a gate bias to the photodetector, where the Al_2O_3 film acts as the gate dielectric and the Au/Si as the gate electrode. Here, we benchmark the TiO_2/Au substrate against the commonly used SiO_2/Si substrate, where the SiO_2 layer with thickness t_s acts as the insulator.

First, we conducted optical simulations to design the TiO_2/Au optical cavity substrate and evaluate its performance. Figure 1b plots the electric field intensity (normalized to the incident intensity) at the substrate surface in the absence of the 2D material for the SiO_2/Si ($t_s = 300$ nm) substrate and TiO_2/Au substrate with varying spacer thickness. As expected, the peak intensity wavelength redshifts with an increase in the spacer thickness. The light intensity is considerably higher on the TiO_2/Au substrate in comparison with the SiO_2/Si substrate. For instance, at the peak intensity wavelength of 6.9 μm for the TiO_2/Au ($t_s =$ 800 nm) substrate, the light intensity is 10.4 times larger on the TiO_2/Au substrate than that on the SiO_2/Si substrate.

To further illustrate this, Figure 1c and 1d present the distribution of the electric field intensity in the cross section of the TiO_2/Au ($t_s = 800$ nm) and SiO_2/Si ($t_s = 300$ nm) substrates, respectively, in the absence of the 2D material at $\lambda = 6.9$ μm. The surface of the substrate at $y = 0$ is marked by a red dashed line. These profiles indicate that for the TiO_2/Au substrate with proper spacer thickness, the maximum intensity ($|E|^2/|E_i|^2 = 3.76$) lies at the substrate surface, while for the SiO_2/Si substrate, this maximum ($|E|^2/|E_i|^2 =$ 2.37) occurs at $y = 1.43$ μm (*i.e.*, at 1.43 μm above the substrate surface). It should also be noted that the light intensity at the surface of the SiO_2/Si substrate is smaller than the incident intensity ($|E|^2/|E_i|^2 = 0.36$). This comes from the destructive interference between the incident and reflected waves at the substrate surface.

It is noteworthy that the electric field intensity at the surface of the SiO_2/Si substrate can also be optimized in the MWIR region by adjusting the SiO_2 thickness, as shown in Figure 1e. However, as observed in this figure, SiO_2/Si is not an appropriate substrate for the LWIR

region, since the high absorption of SiO_2 at these wavelengths leads to low light intensity at the substrate surface. Furthermore, other studies typically use an SiO_2/Si substrate with SiO_2 thickness of 300 nm[17,23,29,30,32,44] or less[12,14–16,20,22,28,33,34] in the 2D material-based photodetectors, regardless of the operating wavelength. Accordingly, we consider an SiO_2 thickness of 300 nm in the following simulations and experiments.

The time-averaged optical power density absorbed in the 2D material sitting on the substrate can be expressed as[49]

$$\langle \overrightarrow{E(t)} \cdot \frac{\partial \overrightarrow{P(t)}}{\partial t} \rangle = \frac{1}{2}\omega\epsilon''|\vec{E}|^2 = \epsilon_0 \omega n k |\vec{E}|^2$$

where $\vec{E}$ denotes the electric field, $\vec{P}$ electric polarization, ω angular frequency, $\epsilon = \epsilon' + \mathrm{i}\epsilon'' = \epsilon_0(n + \mathrm{i}k)^2$ 2D material's permittivity, and ϵ_0 vacuum permittivity. n and k are the real and imaginary parts of the 2D material refractive index, respectively. According to this equation, the optical power absorbed in the 2D material is proportional to the electric field intensity, n, and k.

The above discussions imply that a thin 2D material with negligible influence on the light intensity distribution, such as monolayer graphene, would absorb ~10.4 times more power on the TiO_2/Au ($t_s = 800$ nm) substrate compared with the SiO_2/Si ($t_s = 300$ nm) substrate at $\lambda = 6.9$ μm. However, this is not true for a thick multilayer 2D material with significant reflection and absorption. Next, we investigate the effect of the thickness (t_{2D}) and complex refractive index ($n + \mathrm{i}k$) of the 2D material on the light absorption in the 2D material sitting on the TiO_2/Au and SiO_2/Si substrates.

Figure 2a presents the optical power (normalized to the source power) absorbed in the 2D material sitting on the TiO_2/Au ($t_s = 800$ nm) substrate as a function of wavelength for different t_{2D}, n, and k values. The absorbed power was obtained by calculating the net power flow into a surface enclosing the 2D material. It is observed that the 2D material absorption increases with an increase in its thickness. There is also a redshift in the peak

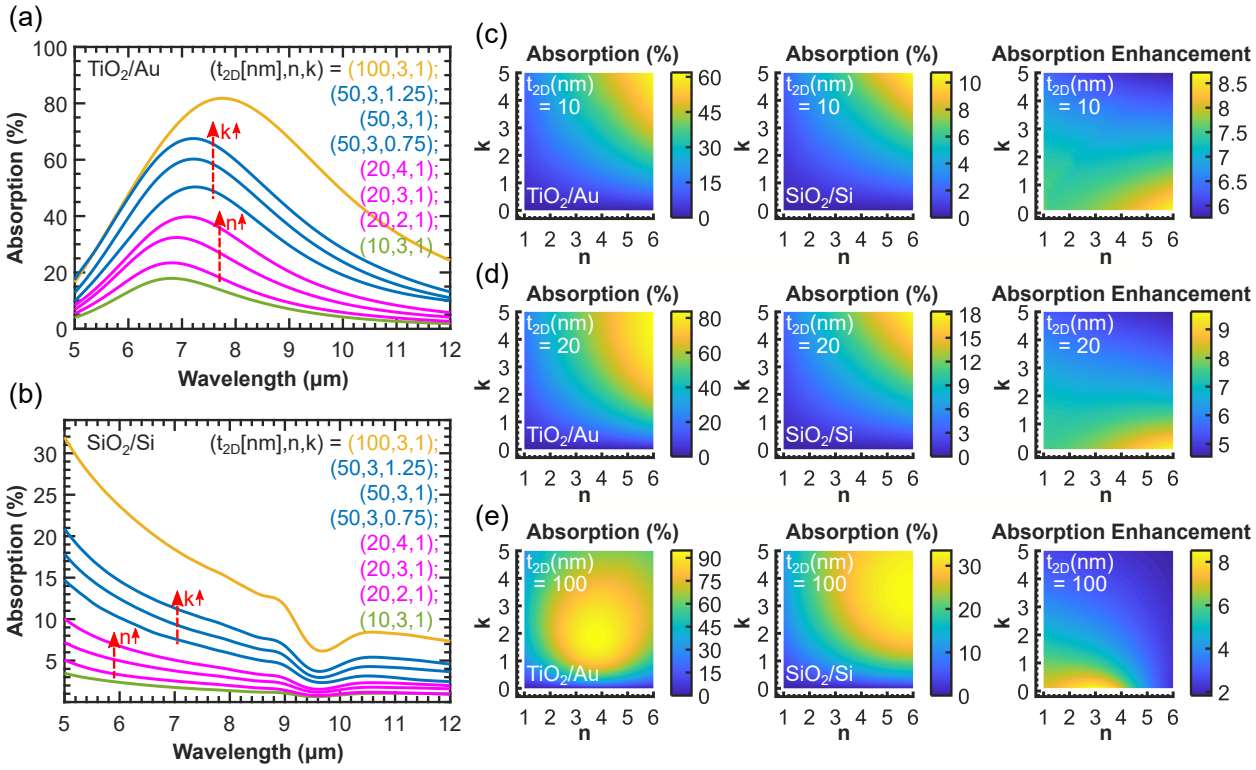

Figure 2: (a) and (b) Optical power absorbed in the 2D material lying on the TiO_2/Au (t_s = 800 nm) and SiO_2/Si (t_s = 300 nm) substrates, respectively, with varying thickness (t_{2D}) and refractive index (n and k) of the 2D material. (c)–(e) Optical power absorbed and absorption enhancement in the 2D material lying on the TiO_2/Au (t_s = 800 nm) and SiO_2/Si (t_s = 300 nm) substrates as functions of n and k with t_{2D} = 10, 20, and 100 nm, respectively, at $\lambda = 8.35$ μm. The absorption enhancement is defined as the ratio of the 2D material absorption with the TiO_2/Au substrate to that with the SiO_2/Si substrate.

absorption wavelength with the increase in thickness. At constant thickness, larger n and larger k values lead to larger absorption. Also, there is a redshift and a blue shift in the peak absorption wavelength with the increase in n and k, respectively. The optical power absorbed in the 2D material on the SiO_2/Si (t_s = 300 nm) substrate is plotted in Figure 2b for the same t_{2D}, n, and k values as Figure 2a. Here again, the power absorbed in the 2D material increases with an increase in its thickness and refractive index values. Also, we note that the 2D material absorption is greater on the TiO_2/Au than that on the SiO_2/Si substrate over a wide wavelength range.

To further study the 2D material absorption enhancement provided by the TiO_2/Au substrate, Figure 2c–e illustrate the power absorbed and absorption enhancement in the

2D material at $\lambda = 8.35$ μm for a wide range of n and k values on the TiO_2/Au ($t_s =$ 800 nm) and SiO_2/Si ($t_s = 300$ nm) substrates for $t_{2D} = 10$, 20, and 100 nm, respectively. The same results for $t_{2D} = 50$ nm are shown in the Supporting Information, Figure S1. Here, the absorption enhancement is defined as the ratio of the 2D material absorption with the TiO_2/Au substrate to that with the SiO_2/Si substrate. The absorption increases almost monotonically with an increase in n and k for $t_{2D} = 10$ and 20 nm for both substrates. However, this is not the case for the thicker 2D materials ($t_{2D} = 50$ and 100 nm); for instance, the 100-nm-thick 2D material on the TiO_2/Au substrate has a maximum absorption of 94.8% at $(n, k) = (3.75, 1.75)$. Regardless of t_{2D}, the absorption enhancement is maximum for low-absorbance materials (small k values), and it drops with an increase in k. Also, the absorption enhancement is generally higher for thinner 2D materials. Here we observe a maximum absorption enhancement of 9.6 for $(n, k) = (6, 0.1)$ for $t_{2D} = 20$ nm and a minimum absorption enhancement of 1.84 for $(n, k) = (6, 5)$ for $t_{2D} = 100$ nm.

Next, we fabricated and characterized $PtSe_2$ photoconductors on TiO_2/Au ($t_s = 800$ nm) and SiO_2/Si ($t_s = 300$ nm) substrates. The stable octahedral 1T crystal structure of $PtSe_2$ is depicted in Figure 3a. $PtSe_2$ layers are stacked in the AA arrangement, as shown in Figure 3b, to form multilayer $PtSe_2$.[29] Here, $PtSe_2$ photodetectors were prepared by the mechanical exfoliation of the $PtSe_2$ flakes onto the substrate, followed by the pattering and deposition of the Cr/Au source and drain electrodes. Multilayer $PtSe_2$ flakes with thicknesses in the range of ~10–70 nm were chosen for the fabrication of these photodetectors. $PtSe_2$ flakes thinner than ~10 nm and large enough for device fabrication (≥ 3 μm) were very scarce. Figure 3c presents an optical microscope image of a $PtSe_2$ photodetector on the TiO_2/Au substrate. An atomic force microscope (AFM) image of this $PtSe_2$ flake is included in Figure 3d, which shows that this flake has an uneven thickness ranging from 56 to 71 nm. The drain current-gate voltage (I_d-V_g) characteristic of this device is shown in Figure 3e. The drain-source voltage (V_d) was kept at 50 mV. Multilayer $PtSe_2$ is a semi-metallic material; hence, there is no obvious gate control over drain current. Nonetheless, we observed weak p-type

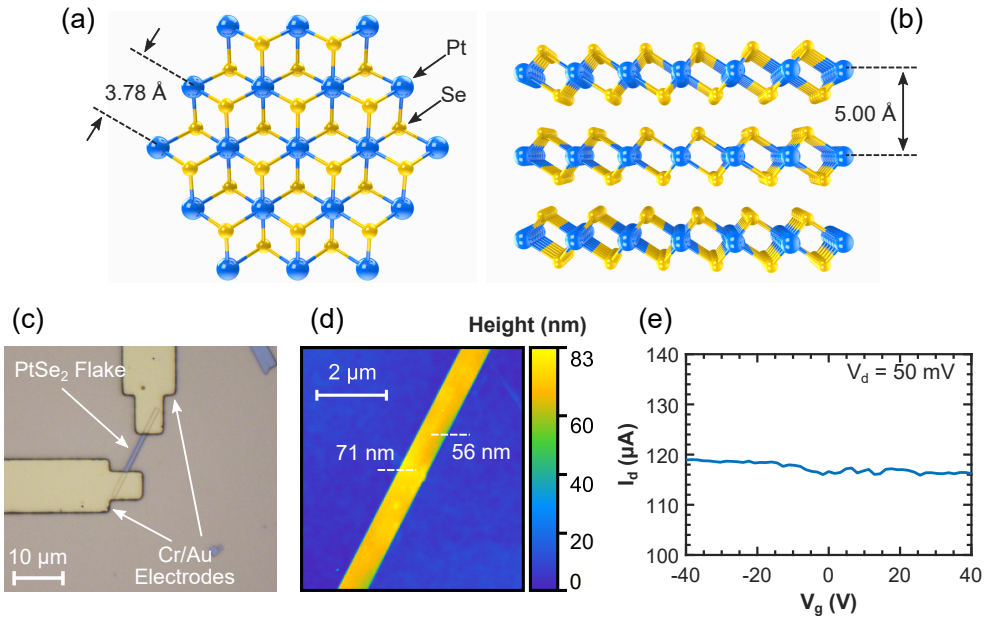

Figure 3: (a) Top and (b) side views of the multilayer 1T-$PtSe_2$ crystal structure with AA stacking order. (c) Optical micrograph of a $PtSe_2$ photodetector fabricated on the TiO_2/Au (t_s = 800 nm) optical cavity substrate. (d) Atomic force micrograph of the $PtSe_2$ flake in panel c. (e) Drain current *vs.* gate voltage characteristic of the $PtSe_2$ device.

and ambipolar behavior in few-layer $PtSe_2$ flakes with thicknesses below 5 nm. Figure S2 in the Supporting Information displays examples of I_d-V_g characteristics of few-layer $PtSe_2$ flakes on the SiO_2/Si substrate.

The photoresponse of the $PtSe_2$ device on the TiO_2/Au (t_s = 800 nm) substrate to the LWIR laser (λ = 8.35 μm) is shown in Figure 4a, where the laser was pulsed at 700 Hz and the incident power density was 43.5 W/cm^2. The drain bias was V_d = 50 mV, and the gate electrode was disconnected. All measurements were taken at room temperature unless stated otherwise. A photocurrent ($I_{ph} = I_{light} - I_{dark}$) of 184 nA is observed. Figure 4b plots the photocurrent as a function of laser power density for this device. We observe a linear behavior, which is desirable for photodetectors. The responsivity of a photodetector is defined as $R = I_{ph}/P_{in}$, where P_{in} is the power incident on the device. Figure 4c shows the responsivity of this device as a function of laser power density. A maximum responsivity of 54.3 mA/W is measured. The detectivity, which represents the photodetector's ability to

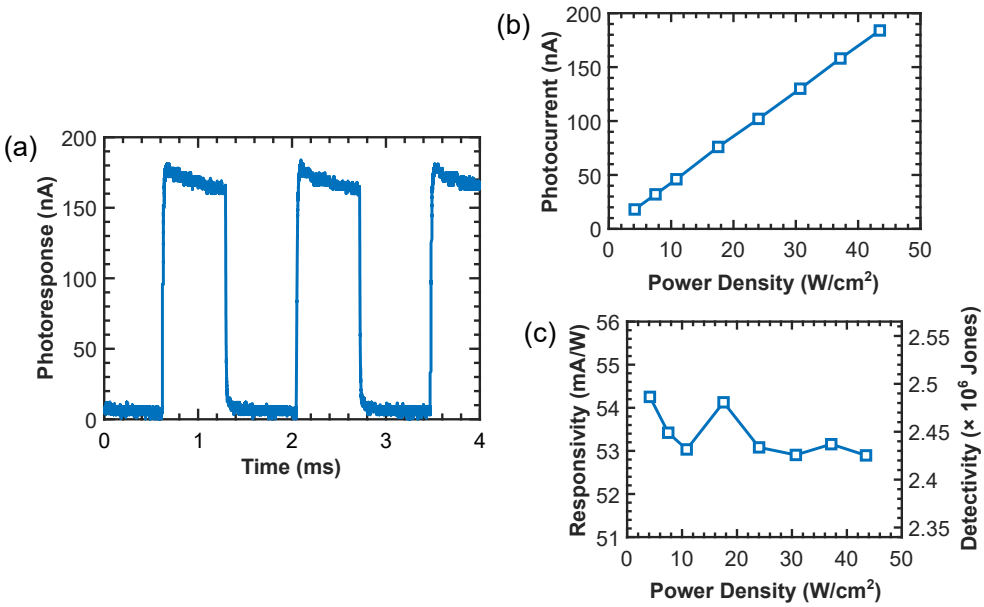

Figure 4: Photoresponse of a $PtSe_2$ photodetector on the TiO_2/Au ($t_s = 800$ nm) substrate to the 8.35-μm laser. (a) Photoresponse with the laser modulated at 700 Hz at the incident power density of 43.5 W/cm^2. (b) Photocurrent as a function of laser power density. (c) Responsivity and detectivity as functions of laser power density. The drain bias was V_d = 50 mV, and the gate electrode was disconnected in the above measurements.

differentiate the signal from noise, is defined as

$$D^* = \frac{\sqrt{A\ \Delta f}}{NEP} = \frac{R\sqrt{A\ \Delta f}}{\sqrt{\bar{I}_n^2}}$$

where A is the device area, Δf sampling bandwidth, NEP noise equivalent power, R responsivity, and I_n noise current. Assuming that the total noise of the photodetector is dominated by the shot noise from the dark current, the noise current can be approximated as $\bar{I}_n^2 \approx 2eI_{dark}\Delta$f.[5,24] This leads us to

$$D^* \approx \frac{R\sqrt{A}}{\sqrt{2eI_{dark}}}$$

where e is the unit charge and I_{dark} is the dark current. The detectivity of this device, calculated using the latter equation, is reported in Figure 4c. It shows a maximum detectivity of 2.5×10^6 Jones (cm$\sqrt{\text{Hz}}$/W).

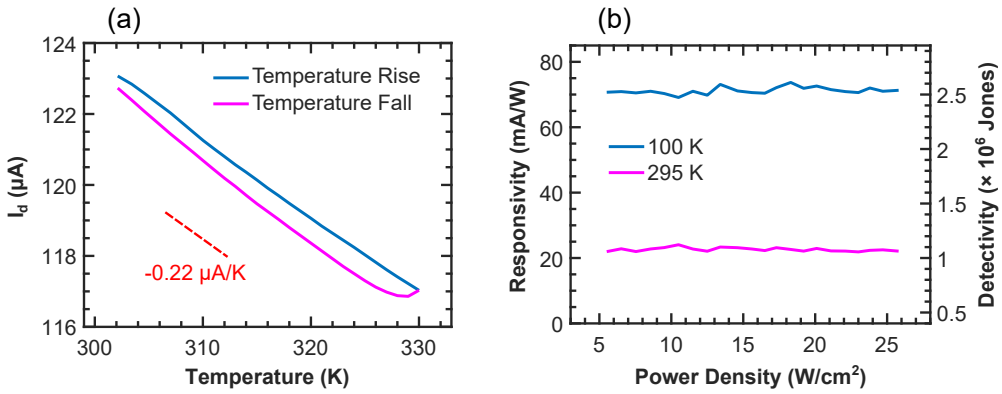

Figure 5: (a) Drain current as a function of temperature for a $PtSe_2$ device on the SiO_2/Si (t_s = 300 nm) substrate in the dark. (b) Responsivity and detectivity of a $PtSe_2$ photodetector on the TiO_2/Au (t_s = 800 nm) substrate to the 8.35-μm laser as functions of laser power density at room and cryogenic temperatures. The drain bias was V_d = 50 mV, and the gate electrode was disconnected in the above measurements.

To understand the photodetection mechanism in these devices, we studied the temperature dependence of the drain current in the dark. Figure 5a plots the dark current as a function of temperature for a $PtSe_2$ device on the SiO_2/Si (t_s = 300 nm) substrate. The same type of measurement for another device is shown in the Supporting Information, Figure S3. As expected for a semi-metallic material, the current decreases with an increase in temperature. This is consistent with the findings of ref. 29. Hence, the photoresponse does not originate from the temperature rise induced by the illumination (bolometric effect), and is instead attributed to the generation of photocarriers and their collection by the electrodes (photoconductive effect). The effect of cryogenic cooling on device performance was also investigated. Figure 5b plots the responsivity and detectivity of a $PtSe_2$ photodetector on the TiO_2/Au (t_s = 800 nm) substrate to the 8.35-μm laser at different temperatures. Both the light and dark currents increase as the device is cooled down from 295 to 100 K. The dark current increases from 162 to 294 μA. The photocurrent and responsivity are enhanced by 3.15 times and detectivity by 2.34 times.

Several $PtSe_2$ photodetectors were fabricated on the TiO_2/Au (t_s = 800 nm) and SiO_2/Si (t_s = 300 nm) substrates. The responsivity and detectivity of these devices to the 8.35-μm laser are compared in Figure 6a and 6b, respectively. Each bar represents a device.

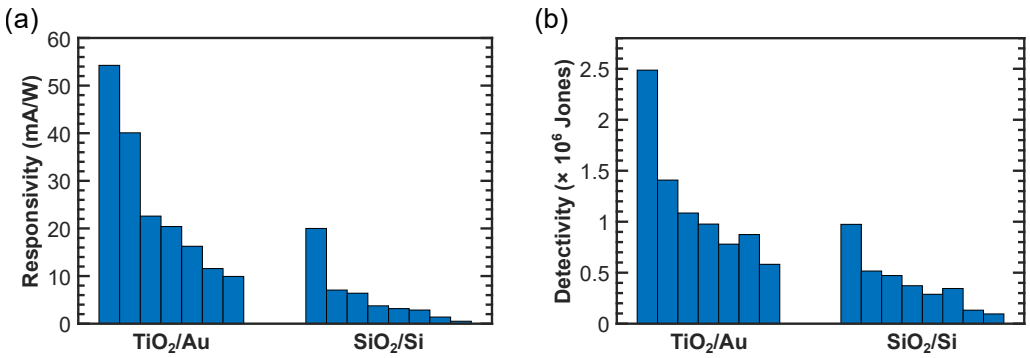

Figure 6: (a) Responsivity and (b) detectivity of different $PtSe_2$ devices to the 8.35-μm light on the TiO_2/Au (t_s = 800 nm) and SiO_2/Si (t_s = 300 nm) substrates. Each bar represents a device. The drain bias was V_d = 50 mV, and the gate electrode was disconnected in the above measurements.

As expected, the photodetectors on the TiO_2/Au substrate generally perform better than those on the SiO_2/Si substrate. The responsivity and detectivity of the best device on the TiO_2/Au substrate are respectively 2.7 and 2.6 times higher than those of the best device on the SiO_2/Si substrate. Also, the average values of responsivity and detectivity for the devices on the TiO_2/Au substrate are respectively 4.5 and 3 times higher than those for the devices on SiO_2/Si.

As shown in Figure 6a, the best device on the SiO_2/Si substrate shows a responsivity of 20 mA/W to the LWIR light (λ = 8.35 μm). We also measured the response of this device to visible (λ = 532 nm) and SWIR (λ = 1550 nm) light; the results are plotted in Figure 7a. The visible and SWIR laser beams were chopped at 700 Hz. This device shows responsivity values of 2.1 mA/W and 1.1 mA/W to the 532-nm and 1550-nm light, respectively.

The rise/fall times of the photoresponse plotted in Figure 4a and 7a are limited by the measurement setup, *i.e.*, the speed of the laser in Figure 4a and the chopping process in Figure 7a, rather than the photodetector speed. To characterize the response time of the $PtSe_2$ photodetectors, a device on the SiO_2/Si substrate was illuminated by a pulsed white light source (λ = 450–2400 nm) with a pulse width of $\sim$2 ns. Figure 7b presents the photoresponse of the device, together with the analog pulse signal of the laser. This device responds to the light pulse with a time constant of 54 ns. From another viewpoint, the

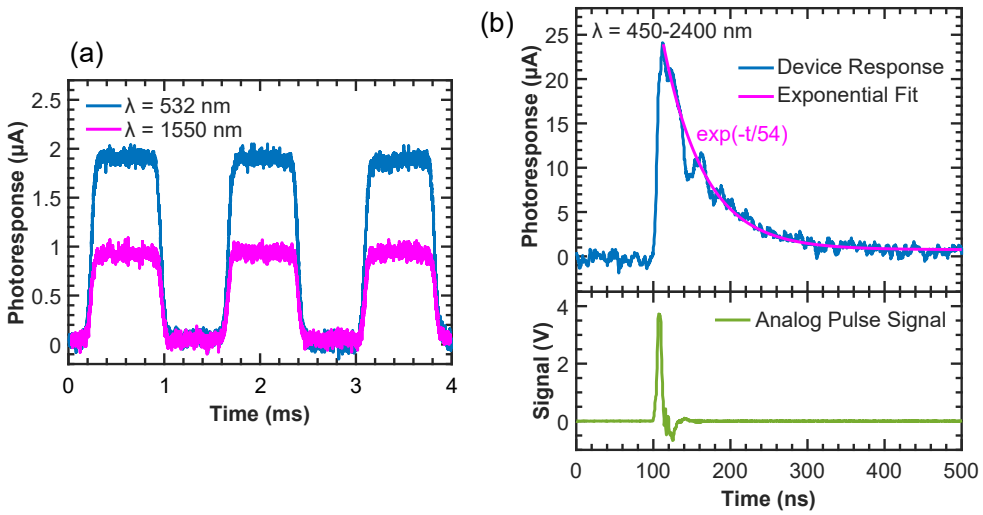

Figure 7: (a) Photoresponse of a $PtSe_2$ photodetector on the SiO_2/Si ($t_s = 300$ nm) substrate to 532-nm and 1550-nm lasers at incident power densities of 5661 and 5242 W/cm^2, respectively. The laser beams were chopped at 700 Hz. (b) Photoresponse of a $PtSe_2$ photodetector on the SiO_2/Si ($t_s = 300$ nm) substrate to the pulsed white light ($\lambda = 450$–2400 nm) laser with a pulse width of 2 ns, along with the analog pulse signal of the laser. The drain bias was $V_d = 50$ mV, and the gate electrode was disconnected in the above measurements.

impulse response of the photodetector decays exponentially, *i.e.*, $e^{-t/\tau}$, where $\tau \approx 54$ ns is the recombination lifetime of the photogenerated carriers.[50]

Conclusion

In summary, we demonstrated fast and broadband (visible to LWIR) photodetectors based on multilayer $PtSe_2$, which was mechanically exfoliated from standard CVT-grown crystals. Moreover, we designed and fabricated an optical cavity substrate to boost the light-matter interaction in 2D materials in the LWIR spectral region. We employed this TiO_2/Au optical cavity substrate to enhance the performance of $PtSe_2$ photodetectors. These devices show a maximum responsivity of 54 mA/W and detectivity of 2.5×10^6 Jones to LWIR illumination (at a wavelength of 8.35 μm) at room temperature. Higher responsivity and detectivity values were reported in ref. 28 for bilayer $PtSe_2$ containing Se vacancies. Our devices, however, are much faster and more practical from a manufacturing perspective. 2D materials have shown great potential for IR photodetection lately, and this study highlights the significant effect

of the substrate on the performance of these devices.

Methods

Simulation. Maxwell's equations were solved employing the finite-difference time-domain (FDTD) technique,[51] implemented in the Lumerical FDTD Solutions software package. The light source was a broadband (λ = 5–13 μm) linearly polarized plane wave at normal incidence. Perfectly matched layers (PMLs) were utilized to describe the boundary conditions in the light propagation direction. Periodic boundary conditions were implemented in the direction perpendicular to light propagation. The mesh size was 1 nm around the finest features. The wavelength-dependent complex refractive index values of TiO_2, Al_2O_3, and SiO_2 were taken from ref. 52, and those of Au and Si were taken from ref. 53.

Fabrication. The fabrication of the TiO_2/Au optical cavity substrate started with e-beam evaporation of a 20/120-nm Cr/Au reflector on a Si substrate. Next, a 1-nm Ti layer was e-beam evaporated to act as the seed layer for the TiO_2 deposition. This was followed by the deposition of the 800-nm TiO_2 spacer *via* reactive sputtering physical vapor deposition. Finally, a 30-nm Al_2O_3 insulator film was deposited using atomic layer deposition (ALD). For the SiO_2/Si substrate, the thermally grown SiO_2 insulator layer was 300-nm-thick.

Chemical vapor transport (CVT)-grown $PtSe_2$ crystals were purchased from HQ Graphene. $PtSe_2$ flakes were deposited onto the substrate by exfoliating the crystals using a sticky tape. Next, the source/drain electrodes (Cr/Au 20/80 nm) were fabricated using the photolithography/e-beam evaporation/lift-off method. Subsequently, the thickness of the $PtSe_2$ flakes was measured using an atomic force microscope (Cypher AFM, Asylum Research) in tapping mode. Finally, the chips were wire-bonded into chip carriers for electrical and optical characterization.

Characterization. The electrical characteristics were measured using a pair of source measure units (2450 SourceMeter, Keithley Instruments) in a two-probe configuration. In

the photoresponse experiments, the 8.35-μm quantum cascade laser (QCL) was directly modulated at 700 Hz. The beams from 532-nm and 1550-nm laser diodes were mechanically chopped at 700 Hz. A thermal power sensor (S401C, Thorlabs) was used to measure the optical power of the lasers. The spot sizes of the lasers were measured using the knife-edge method and the power meter, and thus the power densities were obtained. The signal from the photodetector was amplified using a low-noise current preamplifier (SR570, Stanford Research Systems), and the output was monitored on an oscilloscope. The drain bias was applied using the current preamplifier. Temperature-dependent measurements were taken in a customized cryostat (Janis Research) with a ZnSe window. The response time was characterized by illuminating the device with 2-ns-wide pulses from a supercontinuum white light laser (SuperK Compact, NKT Photonics). A high-speed current amplifier (DHPCA-100, FEMTO) with bandwidth of $\sim$170 MHz was used in this case.

Acknowledgement

This work was supported by the Defense Advanced Research Projects Agency (HR0011-16-1-0004) and by the Australian Research Council (DP180104141 and DP210103428). It was performed in part at the Melbourne Centre for Nanofabrication (MCN) in the Victorian Node of the Australian National Fabrication Facility (ANFF).

Supporting Information

The Supporting Information is available free of charge at http://pubs.acs.org.

Optical power absorbed in the 50-nm-thick 2D material, I_d-V_g characteristics of few-layer $PtSe_2$ devices, temperature dependence of dark current for a $PtSe_2$ device.

References

1. Zhuge, F.; Zheng, Z.; Luo, P.; Lv, L.; Huang, Y.; Li, H.; Zhai, T. Nanostructured Materials and Architectures for Advanced Infrared Photodetection. *Adv. Mater. Technol.* **2017**, *2*, 1700005.

2. Rogalski, A. HgCdTe Infrared Detector Material: History, Status and Outlook. *Rep. Prog. Phys.* **2005**, *68*, 2267.

3. Norton, P. HgCdTe Infrared Detectors. *Opto-Electron. Rev.* **2002**, *10*, 159–174.

4. Downs, C.; Vandervelde, T. E. Progress in Infrared Photodetectors Since 2000. *Sensors* **2013**, *13*, 5054–5098.

5. Xie, C.; Mak, C.; Tao, X.; Yan, F. Photodetectors Based on Two-Dimensional Layered Materials beyond Graphene. *Adv. Funct. Mater.* **2017**, *27*, 1603886.

6. Koppens, F. H. L.; Mueller, T.; Avouris, P.; Ferrari, A. C.; Vitiello, M. S.; Polini, M. Photodetectors Based on Graphene, Other Two-Dimensional Materials and Hybrid Systems. *Nat. Nanotechnol.* **2014**, *9*, 780–793.

7. Wang, F.; Zhang, Y.; Gao, Y.; Luo, P.; Su, J.; Han, W.; Liu, K.; Li, H.; Zhai, T. 2D Metal Chalcogenides for IR Photodetection. *Small* **2019**, *15*, 1901347.

8. Sun, Z.; Chang, H. Graphene and Graphene-Like Two-Dimensional Materials in Photodetection: Mechanisms and Methodology. *ACS Nano* **2014**, *8*, 4133–4156.

9. Azar, N. S.; Shrestha, V. R.; Crozier, K. B. Bull's Eye Grating Integrated with Optical Nanoantennas for Plasmonic Enhancement of Graphene Long-Wave Infrared Photodetectors. *Appl. Phys. Lett.* **2019**, *114*, 091108.

10. Wang, H.; Li, S.; Ai, R.; Huang, H.; Shao, L.; Wang, J. Plasmonically Enabled Two-Dimensional Material-Based Optoelectronic Devices. *Nanoscale* **2020**, *12*, 8095–8108.

11. Chen, H.; Liu, H.; Zhang, Z.; Hu, K.; Fang, X. Nanostructured Photodetectors: From Ultraviolet to Terahertz. *Adv. Mater.* **2016**, *28*, 403–433.

12. Cakmakyapan, S.; Lu, P. K.; Navabi, A.; Jarrahi, M. Gold-Patched Graphene Nano-Stripes for High-Responsivity and Ultrafast Photodetection from the Visible to Infrared Regime. *Light Sci. Appl.* **2018**, *7*, 1–9.

13. Liu, N.; Tian, H.; Schwartz, G.; Tok, J. B.-H.; Ren, T.-L.; Bao, Z. Large-Area, Transparent, and Flexible Infrared Photodetector Fabricated Using *P-N* Junctions Formed by *N*-Doping Chemical Vapor Deposition Grown Graphene. *Nano Lett.* **2014**, *14*, 3702–3708.

14. Freitag, M.; Low, T.; Zhu, W.; Yan, H.; Xia, F.; Avouris, P. Photocurrent in Graphene Harnessed by Tunable Intrinsic Plasmons. *Nat. Commun.* **2013**, *4*, 1–8.

15. Yao, Y.; Shankar, R.; Rauter, P.; Song, Y.; Kong, J.; Loncar, M.; Capasso, F. High-Responsivity Mid-Infrared Graphene Detectors with Antenna-Enhanced Photocarrier Generation and Collection. *Nano Lett.* **2014**, *14*, 3749–3754.

16. Chen, Z.; Li, X.; Wang, J.; Tao, L.; Long, M.; Liang, S.-J.; Ang, L. K.; Shu, C.; Tsang, H. K.; Xu, J.-B. Synergistic Effects of Plasmonics and Electron Trapping in Graphene Short-Wave Infrared Photodetectors with Ultrahigh Responsivity. *ACS Nano* **2017**, *11*, 430–437.

17. Mueller, T.; Xia, F.; Avouris, P. Graphene Photodetectors for High-Speed Optical Communications. *Nat. Photonics* **2010**, *4*, 297–301.

18. Bullock, J.; Amani, M.; Cho, J.; Chen, Y.-Z.; Ahn, G. H.; Adinolfi, V.; Shrestha, V. R.; Gao, Y.; Crozier, K. B.; Chueh, Y.-L.; Javey, A. Polarization-Resolved Black Phosphorus/Molybdenum Disulfide Mid-Wave Infrared Photodiodes with High Detectivity at Room Temperature. *Nat. Photonics* **2018**, *12*, 601–607.

19. Chen, X.; Lu, X.; Deng, B.; Sinai, O.; Shao, Y.; Li, C.; Yuan, S.; Tran2, V.; Watanabe, K.; Taniguchi, T.; Naveh, D.; Yang, L.; Xia, F. Widely Tunable Black Phosphorus Mid-Infrared Photodetector. *Nat. Commun.* **2017**, *8*, 1–7.

20. Guo, Q.; Pospischil, A.; Bhuiyan, M.; Jiang, H.; Tian, H.; Farmer, D.; Deng, B.; Li, C.; Han, S.-J.; Wang, H.; Xia, Q.; Ma, T.-P.; Mueller, T.; Xia, F. Black Phosphorus Mid-Infrared Photodetectors with High Gain. *Nano Lett.* **2016**, *16*, 4648–4655.

21. Yan, W.; Shrestha, V. R.; Jeangros, Q.; Azar, N. S.; Balendhran, S.; Ballif, C.; Crozier, K. B.; Bullock, J. Spectrally Selective Mid-Wave Infrared Detection Using Fabry-Perot Cavity Enhanced Black Phosphorus 2D Photodiodes. *ACS Nano* **2020**, *14*, 13645–13651.

22. Amani, M.; Regan, E.; Bullock, J.; Ahn, G. H.; Javey, A. Mid-Wave Infrared Photoconductors Based on Black Phosphorus-Arsenic Alloys. *ACS Nano* **2017**, *11*, 11724–11731.

23. Long, M.; Gao, A.; Wang, P.; Xia, H.; Ott, C.; Pan, C.; Fu, Y.; Liu, E.; Chen, X.; Lu, W.; Nilges, T.; Xu, J.; Wang, X.; Hu, W.; Miao, F. Room Temperature High-Detectivity Mid-Infrared Photodetectors Based on Black Arsenic Phosphorus. *Sci. Adv.* **2017**, *3*, e1700589.

24. Amani, M.; Tan, C.; Zhang, G.; Zhao, C.; Bullock, J.; Song, X.; Kim, H.; Shrestha, V. R.; Gao, Y.; Crozier, K. B.; Scott, M.; Javey, A. Solution-Synthesized High-Mobility Tellurium Nanoflakes for Short-Wave Infrared Photodetectors. *ACS Nano* **2018**, *12*, 7253–7263.

25. Tong, L.; Huang, X.; Wang, P.; Ye, L.; Peng, M.; An, L.; Sun, Q.; Zhang, Y.; Yang, G.; Li, Z.; Zhong, F.; Wang, F.; Wang, Y.; Motlag, M.; Wu, W.; Cheng, G. J.; Hu, W. Stable Mid-Infrared Polarization Imaging Based on Quasi-2D Tellurium at Room Temperature. *Nat. Commun.* **2020**, *11*, 1–10.

26. Tan, C.; Amani, M.; Zhao, C.; Hettick, M.; Song, X.; Lien, D.; Li, H.; Yeh, M.; Shrestha, V. R.; Crozier, K. B.; Scott, M. C.; Javey, A. Evaporated Se_xTe_{1-x} Thin Films with Tunable Bandgaps for Short-Wave Infrared Photodetectors. *Adv. Mater.* **2020**, *32*, 2001329.

27. Kempt, R.; Kuc, A.; Heine, T. Two-Dimensional Noble-Metal Chalcogenides and Phosphochalcogenides. *Angew. Chem. Int. Ed.* **2020**, *59*, 9242–9254.

28. Yu, X.; Yu, P.; Wu, D.; Singh, B.; Zeng, Q.; Lin, H.; Zhou, W.; Lin, J.; Suenaga, K.; Liu, Z.; Wang, Q. J. Atomically Thin Noble Metal Dichalcogenide: A Broadband Mid-Infrared Semiconductor. *Nat. Commun.* **2018**, *9*, 1–9.

29. Zhao, Y.; Qiao, J.; Yu, Z.; Yu, P.; Xu, K.; Lau, S. P.; Zhou, W.; Liu, Z.; Wang, X.; Ji, W.; Chai, Y. High-Electron-Mobility and Air-Stable 2D Layered $PtSe_2$ FETs. *Adv. Mater.* **2017**, *29*, 1604230.

30. Wang, Y.; Yu, Z.; Tong, Y.; Sun, B.; Zhang, Z.; Xu, J.-B.; Sun, X.; Tsang, H. K. High-Speed Infrared Two-Dimensional Platinum Diselenide Photodetectors. *Appl. Phys. Lett.* **2020**, *116*, 211101.

31. Wang, Y.; Yu, Z.; Zhang, Z.; Sun, B.; Tong, Y.; Xu, J.-B.; Sun, X.; Tsang, H. K. Bound-States-in-Continuum Hybrid Integration of 2D Platinum Diselenide on Silicon Nitride for High-Speed Photodetectors. *ACS Photonics* **2020**, *7*, 2643–2649.

32. Long, M.; Wang, Y.; Wang, P.; Zhou, X.; Xia, H.; Luo, C.; Huang, S.; Huang, S.; Zhang, G.; Yan, H.; Fan, Z.; Wu, X.; Chen, X.; Lu, W.; Hu, W. Palladium Diselenide Long-Wavelength Infrared Photodetector with High Sensitivity and Stability. *ACS Nano* **2019**, *13*, 2511–2519.

33. Zhang, G.; Amani, M.; Chaturvedi, A.; Tan, C.; Bullock, J.; Song, X.; Kim, H.; Lien, D.-H.; Scott, M. C.; Zhang, H.; Javey, A. Optical and Electrical Properties of Two-Dimensional Palladium Diselenide. *Appl. Phys. Lett.* **2019**, *114*, 253102.

34. Liang, Q.; Wang, Q.; Zhang, Q.; Wei, J.; Lim, S. X.; Zhu, R.; Hu, J.; Wei, W.; Lee, C.; Sow, C.; Zhang, W.; Wee, A. T. S. High-Performance, Room Temperature, Ultra-Broadband Photodetectors Based on Air-Stable $PdSe_2$. *Adv. Mater.* **2019**, *31*, 1807609.

35. Wang, Z.; Wang, P.; Wang, F.; Ye, J.; He, T.; Wu, F.; Peng, M.; Wu, P.; Chen, Y.; Zhong, F.; Xie, R.; Cui, Z.; Shen, L.; Zhang, Q.; Gu, L.; Luo, M.; Wang, Y.; Chen, H.; Zhou, P.; Pan, A. *et al.* A Noble Metal Dichalcogenide for High-Performance Field-Effect Transistors and Broadband Photodetectors. *Adv. Funct. Mater.* **2020**, *30*, 1907945.

36. Ling, X.; Wang, H.; Huang, S.; Xia, F.; Dresselhaus, M. S. The Renaissance of Black Phosphorus. *Proc. Natl. Acad. Sci. U.S.A.* **2015**, *112*, 4523–4530.

37. Pi, L.; Li, L.; Liu, K.; Zhang, Q.; Li, H.; Zhai, T. Recent Progress on 2D Noble-Transition-Metal Dichalcogenides. *Adv. Funct. Mater.* **2019**, *29*, 1904932.

38. Yim, C.; McEvoy, N.; Riazimehr, S.; Schneider, D. S.; Gity, F.; Monaghan, S.; Hurley, P. K.; Lemme, M. C.; Duesberg, G. S. Wide Spectral Photoresponse of Layered Platinum Diselenide-Based Photodiodes. *Nano Lett.* **2018**, *18*, 1794–1800.

39. Xie, C.; Zeng, L.; Zhang, Z.; Tsang, Y.-H.; Luo, L.; Lee, J.-H. High-Performance Broadband Heterojunction Photodetectors Based on Multilayered $PtSe_2$ Directly Grown on a Si Substrate. *Nanoscale* **2018**, *10*, 15285–15293.

40. Xie, C.; Zeng, L.; Zhang, Z.; Tsang, Y.-H.; Luo, L.; Lee, J.-H. Two-Dimensional/Three-Dimensional Schottky Junction Photovoltaic Devices Realized by the Direct CVD Growth of VdW 2D $PtSe_2$ Layers on Silicon. *ACS Appl. Mater. Interfaces* **2019**, *11*, 27251–27258.

41. Wang, L.; Li, J.-J.; Fan, Q.; Huang, Z.-F.; Lu, Y.-C.; Xie, C.; Wu, C.-Y.; Luo, L.-B. A High-Performance Near-Infrared Light Photovoltaic Detector Based on a Multilayered $PtSe_2$/Ge Heterojunction. *J. Mater. Chem. C* **2019**, *7*, 5019–5027.

42. Wu, D.; Wang, Y.; Zeng, L.; Jia, C.; Wu, E.; Xu, T.; Shi, Z.; Tian, Y.; Li, X.; Tsang, Y. H. Design of 2D Layered $PtSe_2$ Heterojunction for the High-Performance, Room-Temperature, Broadband, Infrared Photodetector. *ACS Photonics* **2018**, *5*, 3820–3827.

43. Zhang, Z.-X.; Zeng, L.-H.; Tong, X.-W.; Gao, Y.; Xie, C.; Tsang, Y. H.; Luo, L.-B.; Wu, Y.-C. Ultrafast, Self-Driven, and Air-Stable Photodetectors Based on Multilayer $PtSe_2$/Perovskite Heterojunctions. *J. Phys. Chem. Lett.* **2018**, *9*, 1185–1194.

44. Yuan, J.; Sun, T.; Hu, Z.; Yu, W.; Ma, W.; Zhang, K.; Sun, B.; Lau, S. P.; Bao, Q.; Lin, S.; Li, S. Wafer-Scale Fabrication of Two-Dimensional PtS_2/$PtSe_2$ Heterojunctions for Efficient and Broad Band Photodetection. *ACS Appl. Mater. Interfaces* **2018**, *10*, 40614–40622.

45. Zeng, L.-H.; Lin, S.-H.; Li, Z.-J.; Zhang, Z.-X.; Zhang, T.-F.; Xie, C.; Mak, C.-H.; Chai, Y.; Lau, S. P.; Luo, L.-B.; Tsang, Y. H. Fast, Self-Driven, Air-Stable, and Broadband Photodetector Based on Vertically Aligned $PtSe_2$/GaAs Heterojunction. *Adv. Funct. Mater.* **2018**, *28*, 1705970.

46. Wang, Y.; Li, L.; Yao, W.; Song, S.; Sun, J. T.; Pan, J.; Ren, X.; Li, C.; Okunishi, E.; Wang, Y.-Q.; Wang, E.; Shao, Y.; Zhang, Y. Y.; tao Yang, H.; Schwier, E. F.; Iwasawa, H.; Shimada, K.; Taniguchi, M.; Cheng, Z.; Zhou, S. *et al.* Monolayer $PtSe_2$, a New Semiconducting Transition-Metal-Dichalcogenide, Epitaxially Grown by Direct Selenization of Pt. *Nano Lett.* **2015**, *15*, 4013–4018.

47. Thareja, V.; Kang, J.-H.; Yuan, H.; Milaninia, K. M.; Hwang, H. Y.; Cui, Y.; Kik, P. G.; Brongersma, M. L. Electrically Tunable Coherent Optical Absorption in Graphene with Ion Gel. *Nano Lett.* **2015**, *15*, 1570–1576.

48. Xu, H. Enhanced Light-Matter Interaction of a MoS_2 Monolayer with a Gold Mirror Layer. *RSC Adv.* **2017**, *7*, 23109–23113.

49. Liu, J.-M. *Principles of Photonics*; Cambridge University Press: Cambridge, 2016.

50. Chuang, S. L. *Physics of Optoelectronic Devices*; Wiley: New York City, 1995.

51. Taflove, A.; Hagness, S. C. *Computational Electrodynamics: The Finite-Difference Time-Domain Method*; Artech house: London, 2005.

52. Kischkat, J.; Peters, S.; Gruska, B.; Semtsiv, M.; Chashnikova, M.; Klinkmuller, M.; Fedosenko, O.; Machulik, S.; Aleksandrova, A.; Monastyrskyi, G.; Flores, Y.; Masselink, W. T. Mid-Infrared Optical Properties of Thin Films of Aluminum Oxide, Titanium Dioxide, Silicon Dioxide, Aluminum Nitride, and Silicon Nitride. *Appl. Opt.* **2012**, *51*, 6789–6798.

53. Palik, E. D. *Handbook of Optical Constants of Solids*; Academic press: San Diego, 1998; Vol. 3.

Graphical TOC Entry